IJMMM International Journal of Minerals, Metallurgy and Materials 矿物冶金与材料学报（英文版）

Interpretable machine learning-based stretch formability prediction of magnesium alloys

Xu Qin, Qinghang Wang, Li Wang, Shouxin Xia, Haowei Zhai, Lingyu Zhao, Ying Zeng, Yan Song, and Bin Jiang

Cite this article as:
Xu Qin, Qinghang Wang, Li Wang, Shouxin Xia, Haowei Zhai, Lingyu Zhao, Ying Zeng, Yan Song, and Bin Jiang, Interpretable machine learning-based stretch formability prediction of magnesium alloys, *Int. J. Miner. Metall. Mater.*, 32(2025), No. 8, pp. 1943-1954. https://doi.org/10.1007/s12613-024-3002-9

Articles you may be interested in

IJMMM WeChat

QQ author group

INTERNATIONAL JOURNAL OF
Minerals, Metallurgy and Materials

Volume 32, Number 8, August 2025
Page 1943

Research Article https://doi.org/10.1007/s12613-024-3002-9

Interpretable machine learning-based stretch formability prediction of magnesium alloys

Xu Qin[1], *Qinghang Wang*[1),✉], *Li Wang*[1)], *Shouxin Xia*[1)], *Haowei Zhai*[1)], *Lingyu Zhao*[1)], *Ying Zeng*[2)], *Yan Song*[3)], *and Bin Jiang*[4)]

1) School of Mechanical Engineering, Yangzhou University, Yangzhou 225127, China

2) Key Laboratory of Advanced Technologies of Materials, Ministry of Education, School of Material Science and Engineering, Southwest Jiaotong University, Chengdu 610031, China

3) Department of Components and Materials Test & Evaluation Research Center, China Automotive Engineering Research Institute (CAERI), Chongqing 401122, China

4) National Engineering Research Center for Magnesium Alloys, College of Materials Science and Engineering, Chongqing University, Chongqing 400044, China

(Received: 13 June 2024; revised: 4 September 2024; accepted: 6 September 2024)

Abstract: This study involved the development of an interpretable prediction framework to access the stretch formability of AZ31 magnesium alloys through the combination of the extreme gradient boosting (XGBoost) model with the sparrow search algorithm (SSA). Eleven features were extracted from the microstructures (e.g., grain size (GS), maximum pole intensity (I_{max}), degree of texture dispersion (μ), radius of maximum pole position (r), and angle of maximum pole position (A)), mechanical properties (e.g., tensile yield strength (TYS), ultimate tensile strength (UTS), elongation-to-failure (EL), and strength difference (ΔS)) and test conditions (e.g., sheet thickness (t) and punch speed (v)) in the data collected from the literature and experiments. Pearson correlation coefficient and exhaustive screening methods identified ten key features (not including UTS) as the final inputs, and they enhanced the prediction accuracy of Index Erichsen (IE), which served as the model's output. The newly developed SSA-XGBoost model exhibited an improved prediction performance, with a goodness of fit (R^2) of 0.91 compared with traditional machine learning models. A new dataset (four samples) was prepared to validate the reliability and generalization capacity of this model, and below 5% errors were observed between predicted and experimental IE values. Based on this result, the quantitative relationship between the key features and IE values was established via Shapley additive explanation method and XGBoost feature importance analysis. I_{max}, TYS, EL, r, GS, and ΔS showed a crucial influence on the IE of 10 input features. This work offers a reliable and accurate tool for the prediction of the stretch formability of AZ31 magnesium alloys and provides insights into the development of high-formable magnesium alloys.

Keywords: magnesium alloy; machine learning; microstructure; mechanical property; stretch formability

1. Introduction

Magnesium (Mg) and its alloys are the most promising lightweight metallic materials with broad application prospects in the aerospace, automotive, and medical industries [1]. However, these materials frequently exhibit poor stretch formability at room temperature, which considerably limits their large-scale applications due to their low-symmetry hexagonal close-packed crystal structure [2]. A 2–3 mm Index Erichsen (IE), which is considerably lower than that beyond 15 mm in some aluminum (Al) alloys, was obtained in a strong basal-textured AZ31 alloy sheet [3–5]. Features of materials, particularly microstructural features, e.g., texture and grain size (GS), influence stretch formability. Texture weakening is generally an effective method for the activation of more basal slip systems, and it provides a large strain in the thickness direction [6–8]. The influence of GS on the formability of Mg alloys is a complex and unpredictable phenomenon. Kang *et al*. [9] and Park and Shin [10] pointed out that large GS is beneficial for the enhancement of formability through the increase in the work hardening capacity. This finding was mainly due to the activation of {1012} tensile twins in large grains during the Erichsen cupping test. However, Wei *et al*. [11] argued that grain refinement can activate more nonsubstrate slip systems, which improves formability. Machine learning techniques offer a powerful means of data analysis and enable the identification of potential influencing factors and patterns through the mining of large volumes of experimental data. Nevertheless, thus far, reports on the accurate prediction of stretch formability of Mg alloys are limited, and quantitative analysis of the factors affecting them remains lacking.

Machine learning algorithms, e.g., extreme gradient boosting (XGBoost), artificial neural network (ANN), long

✉ Corresponding author: Qinghang Wang E-mail: wangqinghang@yzu.edu.cn

short-term memory (LSTM), support vector machine (SVM), random forest (RF), and regression tree (RT), have been used in the accurate prediction of the mechanical and corrosion properties of Mg alloys and establishment of the correlations between them and microstructures [12–18]. Zhang *et al*. [15] investigated the relationship between the texture and tensile properties of AZ31 Mg alloys using the ANN model and observed that with the increase in maximum pole intensity (I_{max}) and decrease in texture dispersion (μ), the strength was tremendously enhanced, but the ductility was gradually reduced for AZ31 Mg alloys. Xu *et al*. [14] built high-accuracy SVM and ANN models to predict the yield strength and elongation of AZ31 Mg alloys and optimized the alloying process through the adjustment of the solid-solution parameters and extrusion parameters. The RF algorithm was used in the work of Lu *et al*. [18] to model the calculation of corrosion potentials and currents in Mg alloys, and the results uncovered the mechanism underlying the influence of chemical composition and environmental variables on the corrosion potential and corrosion current of the samples. Therefore, in this work, machine learning was expected to be an useful method for the prediction of the stretch formability of Mg alloys and the quantitative description of the relationship between some factors and the IE value.

This study mainly aimed to accurately forecast the stretch formability of AZ31 Mg alloys via a suitable machine learning model. Through a comparison with the traditional algorithms mentioned above, a reliable XGBoost algorithm was developed by combining it with the sparrow search algorithm (SSA). Various performance metrics, including mean absolute error (MAE), root mean squared error (RMSE), and goodness of fit (R^2), were used to evaluate the prediction performance of the newly developed SSA-XGBoost model. The quantitative relationship among microstructures, mechanical properties, testing conditions, and stretch formability of AZ31 Mg alloys was established and revealed via the Shapley additive explanation (SHAP) method and XGBoost feature importance analysis.

2. Experimental

The workflow of this work (Fig. 1) comprised data collection, feature extraction, feature filtering, modeling, model evaluation, and model validation, with the six different parts covered in Sections 2.1 to 2.6.

2.1. Data collection

To control the variables and avoid the influence of alloying elements and secondary phase particles on the stretch formability of Mg alloys, we collected 116 data on AZ31 alloy sheets from published literature and experiments.

The inputs for the model included 11 parameters, which were divided into three categories:

(1) Microstructures: GS, I_{max}, μ, radius of maximum pole position (r), and angle of maximum pole position (A) [19].

(2) Mechanical properties: average tensile yield strength (TYS), average ultimate tensile strength (UTS), average elongation-to-failure (EL), and the strength difference ΔS (ΔS = UTS – TYS) between average UTS and TYS. The ΔS indicates the work hardening capability of materials. The uniform formula of average TYS, UTS, and EL is expressed as follows [8]:

$$\bar{x} = \frac{x_{0^\circ} + 2x_{45^\circ} + x_{90^\circ}}{4} \tag{1}$$

where $\bar{x}$ represents the average TYS, UTS, or EL; x_{0°, x_{45°, and x_{90° are the corresponding data on alloy sheets tensioned

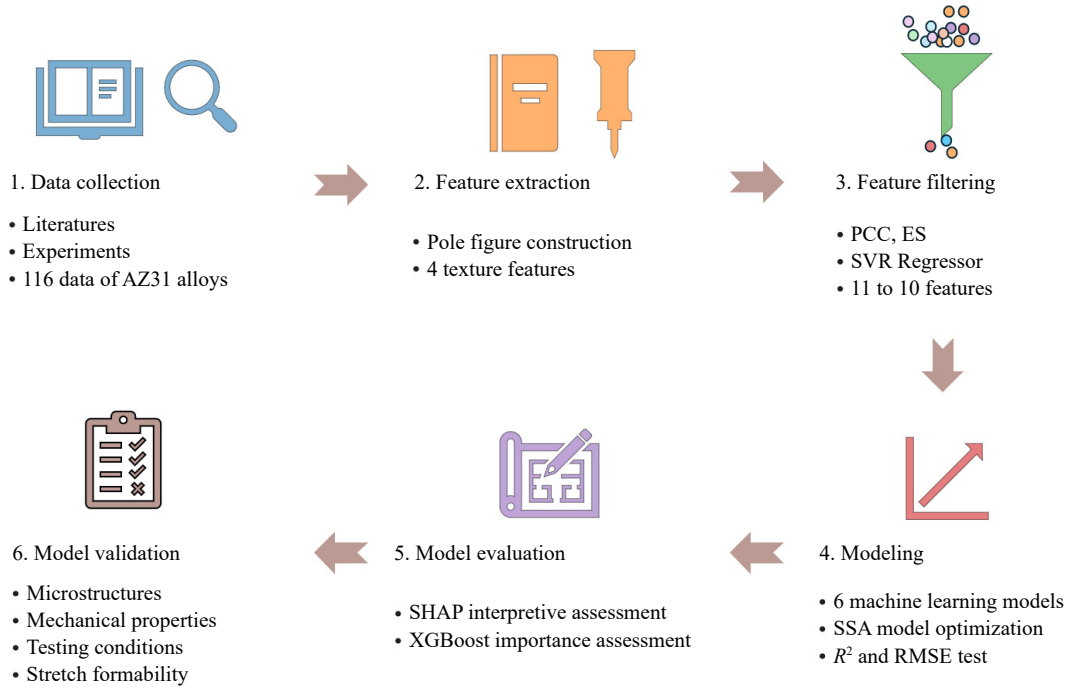

Fig. 1. Flowchart of the prediction of the stretch formability of AZ31 Mg alloys showing six steps, including data collection, feature extraction, feature filtering, modeling, model evaluation, and model validation.

along the 0°, 45°, and 90° inclination toward the extrusion direction (ED) or rolling direction (RD), respectively.

(3) Test conditions: sheet thickness (t) and punch speed (v). Other test conditions, e.g., cup punch diameter, load, and deformation temperature, were constant in the collected literature. Thus, these factors were not considered as variables.

The model output is stretch formability, which is represented by the IE. The values of all the parameters roughly followed a Gaussian distribution (Fig. 2).

2.2. Feature extraction

The four texture features were obtained from the (0001) pole figure of each AZ31 alloy sheet, and the detailed feature-extraction process, with the work of Suh *et al.* [20] as an example, is shown in Fig. 3. The extraction method is as follows:

(1) Image dimensions were uniformly set to 1000×1000 pixels (px). With the use of legends, the original pole intensity $I_0(x,y)$ was determined for each pixel point. Subsequently, the (0001) pole figure was normalized to eliminate dimensional differences between data (Fig. 3(a) and (b)) through Eq. (2):

$$I_1 = \frac{I_0 - I_{\min}}{I_{\max} - I_{\min}} \tag{2}$$

where I_1 and $I_{\min}$ represent the normalized and minimum pole intensities, respectively.

(2) The normalized pole figure was reconstructed based on various color thresholds, which were defined as high- ($I_2 = 0.8$), medium- ($I_2 = 0.4$), and low-density ($I_2 = 0$) regions (Eq. (3)):

$$I_2 = \begin{cases} 0.8, \text{ if } I_1 \geq 0.8 \text{ (high density)} \\ 0.4, \text{ if } 0.4 < I_1 < 0.8 \text{ (middle density)} \\ 0, \text{ if } I_1 \leq 0.2 \text{ (low density)} \end{cases} \tag{3}$$

(3) The texture-related parameters displayed in Fig. 3(c) were calculated to describe the texture characteristics using Eqs. (4)–(7):

$$I_{\max} = \max\left[I_0(x,y)\right] \tag{4}$$

$$\mu = \sqrt{\frac{\sum_{i=1}^{n}\left(I_2 - \overline{I_2}\right)^2}{n-1}} \tag{5}$$

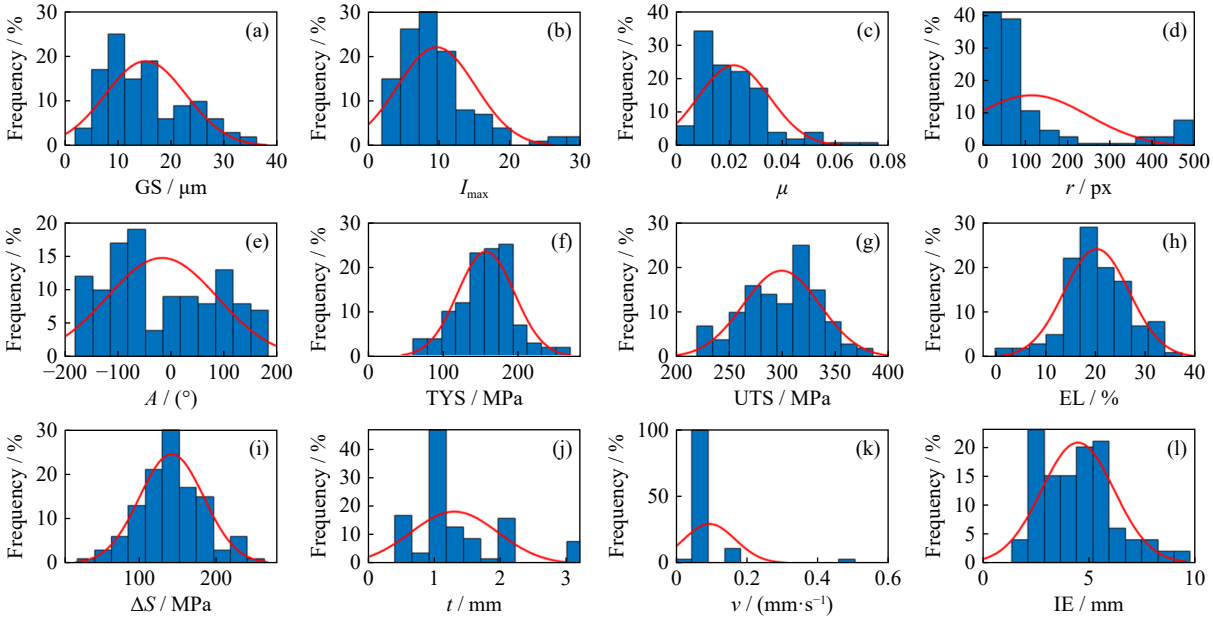

Fig. 2. Distribution maps of parameters in the dataset: (a) GS; (b) I_{max}; (c) μ; (d) r; (e) A; (f) TYS; (g) UTS; (h) EL; (i) ΔS; (j) t; (k) v; (l) IE.

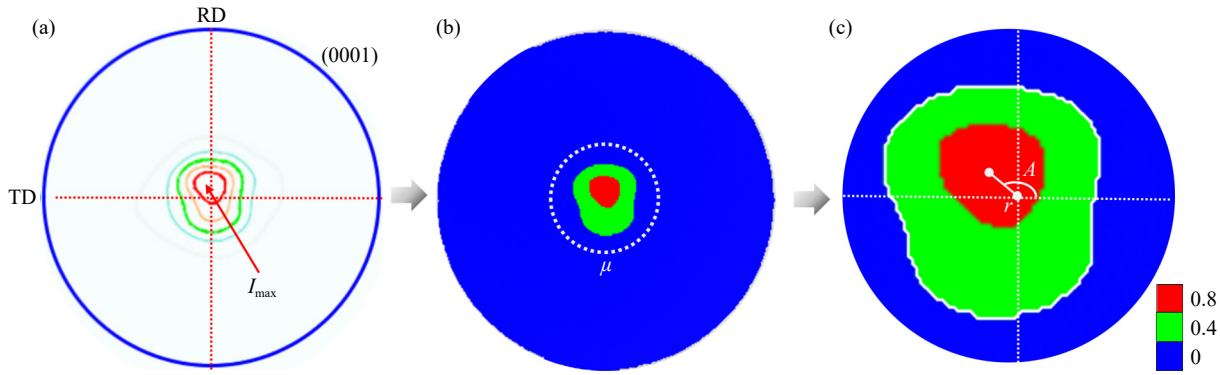

Fig. 3. Texture feature–extraction process: (a) (0001) pole figure; (b) reconstructed (0001) pole figure; (c) high-magnification view of the dotted white circle (b) (0.8, 0.4, and 0 denote high, medium, and low texture density, respectively).

$$r = \sqrt{x_{\max}^2 + y_{\max}^2} \tag{6}$$

$$A = \arctan\left(\frac{y_{\max}}{x_{\max}}\right) (x_{\max} \neq 0) \tag{7}$$

where n refers to the total number of pixels (1000000), $x_{\max}$ and $y_{\max}$ indicate the positions of the pixel with maximum texture intensity, and $\overline{I_2}$ represents the average I_2 of all pixels.

2.3. Feature filtering

Feature filtering was conducted to remove noisy and redundant irrelevant candidate features from the feature space while maintaining important information about the model, which reduced the dimensionality of inputs without losing crucial information for model construction [21]. Given the small initial variable dimensions, a two-step feature filtering process was performed on the candidate features. The Pearson correlation coefficient (PCC) method, which is an indicator of the linear correlation between two features, was initially performed to eliminate redundant features based on Eq. (8) [22]:

$$r_{ab} = \frac{[c\sum(a_i b_i) - \sum a_i \sum b_i]}{\sqrt{\left[c\sum a_i^2 - (\sum a_i)^2\right]\left[c\sum b_i^2 - (\sum b_i)^2\right]}} \tag{8}$$

where c represents the sample size; a_i and b_i represent the ith observed values of two variables, respectively; r_{ab} denotes the value of the two fixed-distance variables. The r_{ab} value was between (–1, 1). The feature filtering threshold was set at 0.95 [22]. When $r_{ab} > 0.95$, the highly correlated features were separately removed from the feature space, and the remaining ones were used as inputs for further screening.

Subsequently, exhaustive screening (ES) was implemented for the systematic evaluation and selection of various possible combinations of features as inputs via a support vector regression (SVR) model for a given modeling task. The combinations of key features with the greatest effect on the stretch formability of alloy sheets were further used in this work.

2.4. Modeling

The inputs comprised the key features obtained through the aforementioned screening process, and the IE served as the output. The regression prediction models were trained using six conventional machine learning algorithms, including XGBoost, ANN, LSTM, SVM, RF, and RT. The model accuracy was evaluated using Eqs. (9)–(11) [23]:

$$\mathrm{MAE} = \frac{1}{m}\sum_{i=1}^{m} |y_i - \hat{y}_i| \tag{9}$$

$$\mathrm{RMSE} = \sqrt{\frac{1}{m}\sum_{i=1}^{m} (y_i - \hat{y}_i)^2} \tag{10}$$

$$R^2 = 1 - \frac{\sum_{i=1}^{m}(y_i - \hat{y}_i)^2}{\sum_{i=1}^{m}(y_i - \bar{y}_i)^2} \tag{11}$$

where y_i represents the true values; $\hat{y}_i$ denotes the model's predicted values; $\bar{y}_i$ indicates the mean of all true values, and m is the number of samples. The best algorithm was selected after model evaluation. The SSA was introduced to further optimize the prediction model accuracy. The SSA exhibits a strong optimization capability and fast convergence speed, and it has been widely applied in fields such as power system optimization, medical image processing, and mechanical design optimization [24].

2.5. Model evaluation

To further explain the mechanism underlying the influence of key features on stretch formability, we used the SHAP method to analyze the contribution of each feature to the prediction value, which was characterized by the SHAP value. The formula for the SHAP value $\phi_i(x)$ of the i-th key feature on the stretch formability is as follows [25]:

$$\phi_i(x) = \sum_{S \subseteq F \setminus \{i\}} \frac{|S|!(|F| - |S| - 1)!}{|F|!} \left[g_{S\cup\{i\}}(x) - g_S(x)\right] \tag{12}$$

where F indicates the set containing all key features, $|F|$ refers to the total number of key features; $S \subseteq F \setminus \{i\}$ represents a subset of all nonzero subsets excluding the i-th key feature; $|S|$ denotes the number of key features in that subset; $g_S(x)$ is the prediction value of the performance model built on the S subset; $g_{S\cup\{i\}}(x)$ corresponds to the prediction value of the performance model built on the S subset plus the i-th key feature; $[g_{S\cup\{i\}}(x) - g_S(x)]$ stands for the contribution of the i-th key feature to the performance prediction; $|S|!(|F| - |S| - 1)!/|F|!$ means the weight coefficient related to the number of key features. A positive or negative $\phi_i(x)$ value indicates the upward or downward effect of the feature value on the model's prediction value, respectively.

In addition, feature importance analysis of the optimal XGBoost model was described; this model can automatically evaluate the importance of each feature to the model's prediction result [26]. The frequency of use of each feature in the model was determined, and the higher the frequency of use, the greater the importance of the corresponding feature.

2.6. Model validation

To verify the reliability and generalization performance of the model, we prepared tensile samples and Erichsen cupping samples from a new dataset prepared from commercial AZ31 as-rolled/as-annealed alloy sheets (Fig. 4). Initially, 3 mm thin pieces were cut at the angles of 0° and 30° away from the normal direction (ND) to the RD of the as-rolled and as-annealed (530°C@3 h) plates (Fig. 4(a)) and labeled as R0, R30, RA0, and RA30. Subsequently, the dog bone-shaped tensile samples were machined at angles of 0°, 45°, and 90° from these thin sheets (Fig. 4(b)). Fig. 4(c) shows the size of each tensile sample with a gauge length of 14 mm and a width of 6 mm. In addition, the square samples with dimensions of 50 mm × 50 mm × 1 mm were fabricated for the Erichsen cupping tests involving the R0, R30, RA0, and RA30 samples (Fig. 4(b) and (c)). Tensile tests were conducted on a CMT6305-300 KN universal testing machine with a strain rate of 10^{-3} s^{-1} at room temperature. Erichsen cupping tests were performed to ascertain the stretch formability of the samples on a GBW-60Z automatic cupping testing machine with a hemispherical punch of a diameter of 20 mm at a

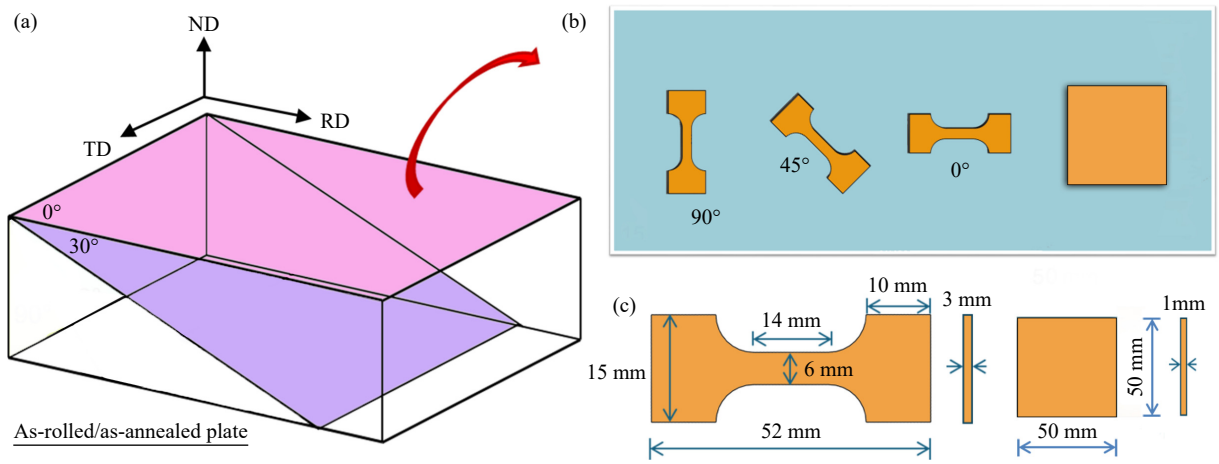

Fig. 4. Schematic of (a) tensile and (b) Erichsen samples cut from commercial AZ31 as-rolled and as-annealed plates, (c) sizes of each tensile sample and Erichsen sample.

speed of 0.05 mm/s and at room temperature. Each test condition necessitated the use of three tensile samples and Erichsen cupping samples to guarantee the reproducibility of experiments.

Electron backscatter diffraction technique (EBSD, JEOL JSM-7800F) was performed to observe the microstructures of all samples in this new dataset. The preparation of EBSD samples comprised grinding, washing, blow-drying, and electropolishing at a voltage of 20 V and an electric current of 0.03 A for 90 s at a temperature of −25°C using a specialized electrolyte called AC2. The step sizes for EBSD scanning were set at 0.5 μm. All EBSD data were subsequently analyzed using Channel 5 software.

3. Results and discussion

3.1. Feature engineering

Fig. 5(a) displays the results of correlation analysis of individual features via the PCC method. For individual features, PCC was used to demonstrate the correlation screening process among 12 features. The findings indicate a strong positive correlation between ΔS, UTS, and TYS, given that ΔS directly reflects the relationship between UTS and TYS. However, no features had a PCC value beyond 0.95, which implies the presence of strong multicollinearity; thus, the removal of any variable at this stage is unnecessary [27].

Fig. 5(b) illustrates the outcome of the ES process. With the increase in the number of feature variables, the RMSE of the model displayed a downward trend and then an upward trend. When the number of input features exceeded 2, the optimal curve (marked by the red line) demonstrated a substantial reduction in the RMSE because additional features provided diverse and supplementary information about the dataset, which enhanced the model's predictive capability and reduced the error. When the number of features increased to 11, the RMSE increased sharply due to the introduction of redundant features. When the number of features was 10, the corresponding model achieved the minimum RMSE of 1.306 through the removal of UTS. This result indicates that the ES method can effectively determine the key features and improve the screening efficiency.

3.2. Model construction and optimization

Fig. 6(a)–(f) shows the results obtained using the training and testing sets for six different algorithms, including XGBoost, ANN, LSTM, SVM, RF, and RT, and the corresponding MAE, RMSE, and R^2 values of the testing set of the models are summarized in Fig. 6(g)–(i). Comparison of the XG-

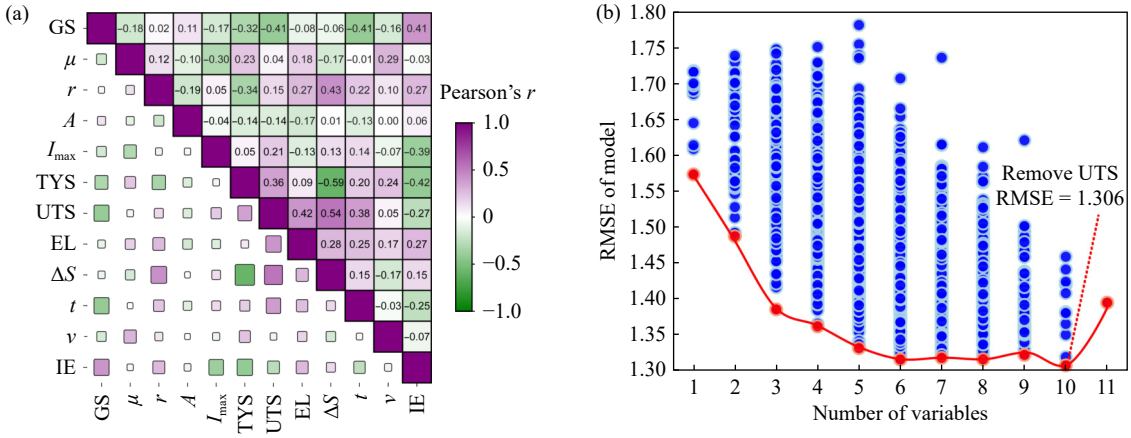

Fig. 5. (a) PCC analysis between features and (b) ES analysis through calculation and comparison of the RMSE of the model at various possible combinations of variables.

Boost model with the other five machine learning models revealed that the XGBoost model had the highest performance prediction accuracy, with the MAE, RMSE, and R^2 values of 0.44, 0.57, and 0.87, respectively. This finding was observed because the XGBoost model can handle high-dimensional feature spaces effectively by integrating multiple decision trees [28]; thus, it demonstrated superior performance in predicting the stretch formability of AZ31 Mg alloys. On the contrary, the other algorithms, such as SVM, RF, and RT, struggled to capture these interactions.

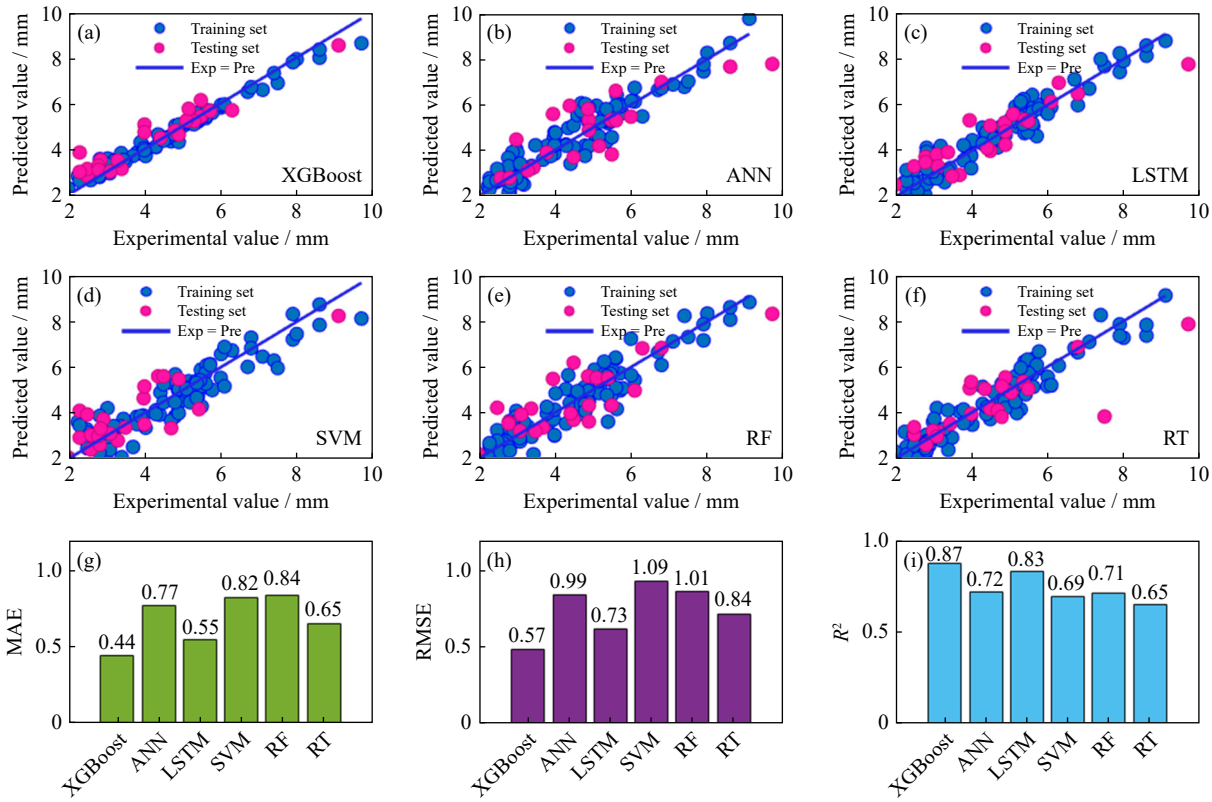

Fig. 6. Model performance of (a) XGBoost, (b) ANN, (c) LSTM, (d) SVM, (e) RF, and (f) RT machine learning algorithms in the prediction of the IE value; evaluation metrics of (g) MAE, (h) RMSE, and (i) R^2.

In the implementation of the XGBoost regression, the correct selection of parameters played a crucial role in ensuring the reliability of prediction results. In general, these parameters, including num_trees, max_depth, eta, and alpha, are manually adjusted during calculations to obtain high goodness-of-fit results. However, the subjective influence introduced by manual control is unavoidable and results in the entrapment of the model in a local optimum [29]. The SSA was introduced to the XGBoost model to address the subjective influence and local optimum problems caused by manual parameter adjustment. Table S1 (see the Supplementary Information) shows the hyperparameters optimized through SSA and their corresponding values. Fig. 7(a) shows the operation process of the SSA-XGBoost model, with the specific steps as follows:

(1) Random data split: the dataset was randomly divided into a training (80% of the data) and a test set (20% of the data).

(2) Fitness function construction: the fitness function used to optimize the XGBoost parameters was constructed based on the RMSE of the prediction model under various optimization iterations. The RMSE value was used as the fitness evaluation metric.

(3) SSA optimization of XGBoost parameters: the SSA was used for the iteratively optimized selection of optimal XGBoost hyperparameters. The fitness of parameter selection was evaluated, and optimization was continued until the iteration conditions were satisfied. The optimal hyperparameters were outputted.

(4) Establishment and evaluation of the SSA-XGBoost model: the SSA-XGBoost model was established using the optimized hyperparameters and evaluated.

The results of the model iteration are presented in Fig. 7(b). The model was run 10 times to prevent accidental errors and ensure the reliability of results. The shaded area represents the error range. Compared with the XGBoost model, the SSA-XGBoost model exhibited a higher R^2 from 0.87 to 0.91, with a relative error of less than 2% across 10 runs. In addition, the RMSE decreased from 0.54 to 0.53, with a relative error of less than 3% across the 10 runs. This finding indicates that the SSA-XGBoost model possesses enhanced capabilities for fitting nonlinear relationships and controlling the dispersion of prediction results. Consequently, the integration of the SSA and XGBoost algorithms validly addressed the limitations of manual parameter adjustment and provided a reliable and efficient approach for the optimization of the XGBoost model parameters and improving the prediction model accuracy.

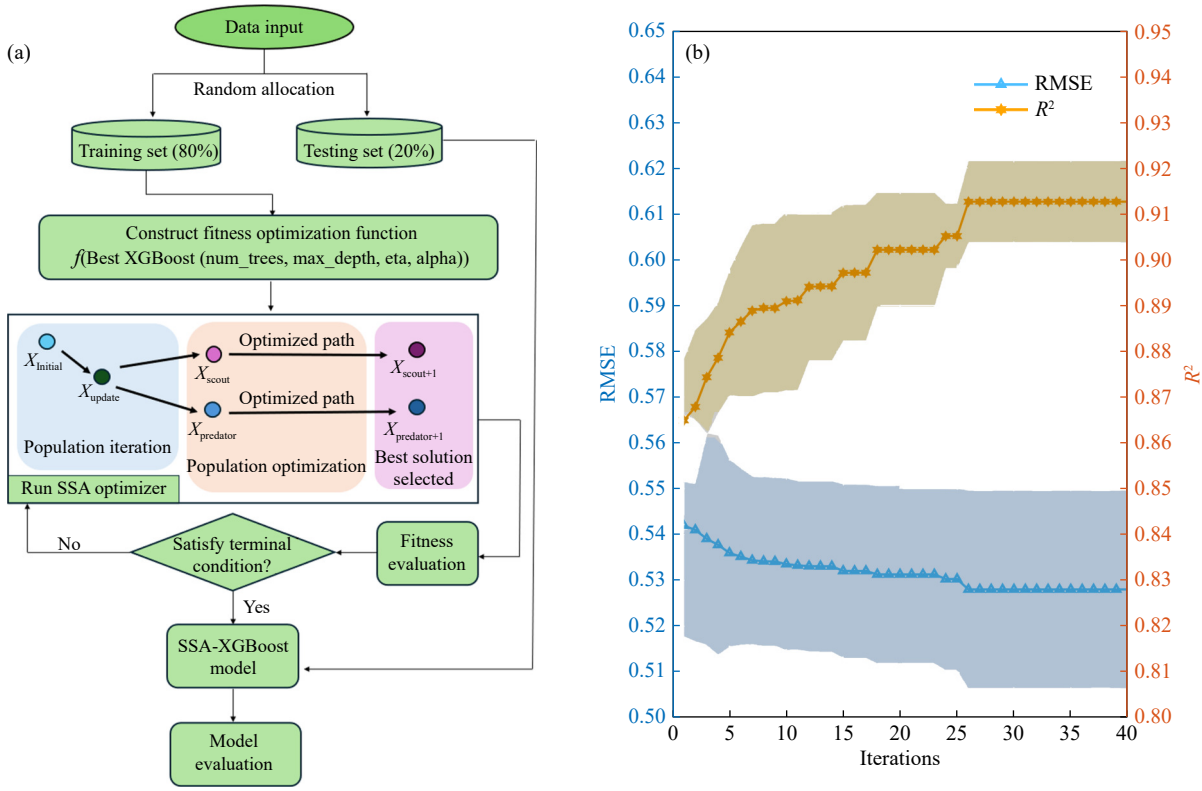

Fig. 7. (a) Operation process of the SSA-XGBoost model and (b) optimal findings obtained using the feedback of RMSE and R^2 through multiple iterations.

3.3. Model interpretation

3.3.1. SHAP interpretive assessment

Fig. 8(a) and (b) illustrates the summary plot of SHAP values and the radar chart of feature contributions, respectively. The *x*-position of scatter points represents the influence of feature values on the model's prediction, and the color of scatter points indicates the magnitude of feature values.

The most significant features that influence the IE regression prediction model include I_{max}, TYS, EL, *r*, GS, and Δ*S*. The effects of *t*, *μ*, *A*, and *v* were relatively smaller. Among these microstructural features, I_{max}, *r*, and GS exhibited the most significant effect on material anisotropy and strain localization, which led to a more pronounced effect on stretch formability. TYS, EL, and Δ*S* directly depend on I_{max}, *r*, and

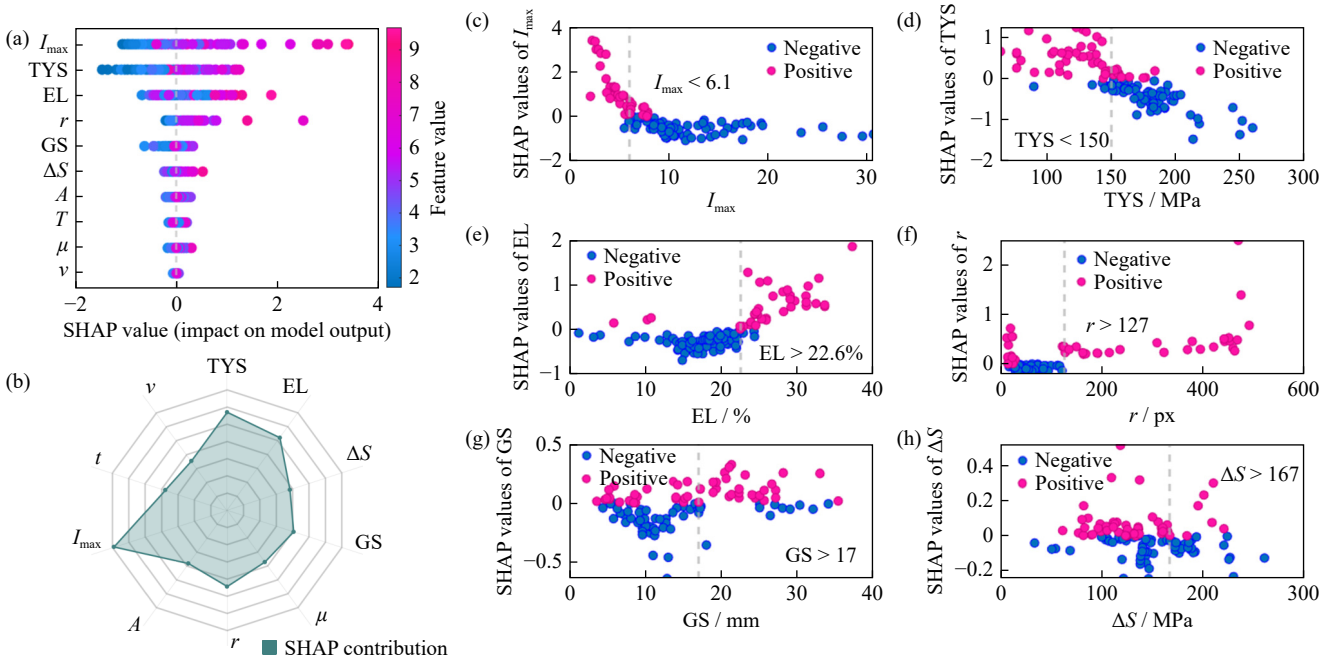

Fig. 8. SHAP analysis of the model: (a) summary plot; (b) radar proportion of each feature. SHAP plots of the top 6 ranked features: (c) I_{max}; (d) TYS; (e) EL; (f) *r*; (g) GS; (h) Δ*S*.

GS in Mg alloys [6–10], which make them the main influencing factors. By contrast, the effect of test conditions (t and v) on stretch formability was relatively less significant, and this finding may be attributed to the minor variations in both factors within the scope of testing, as documented in the collected literature.

Fig. 8(c)–(h) displays the SHAP values of the highest ranking features and their respective feature values. Certain critical values at which the SHAP values were predominantly positive (red points) or negative (blue points) on either side can be identified. When I_{max} < 6.1, the SHAP values were positive (Fig. 8(c)), and with the decrease in I_{max}, a high contribution to the enhancement of stretch formability was observed. This result is highly consistent with those of reported works indicating that the formation of weak texture is beneficial for reducing the plane anisotropy of Mg sheets during deformation through the launch of more basal slip systems and extension twins to accommodate thickness-direction strains [6–8,30]. As TYS < 150 MPa and EL > 22.6%, the corresponding SHAP values were also positive (Fig. 8(d) and (e)). A low TYS and a high EL indicate a reduced low deformation resistance and a high work hardening capacity, which can delay the appearance of microcrack initiation during the Erichsen cupping tests [9,31]. Furthermore, at r > 127 px, with the increase in r, the SHAP value was in direct proportion to it (Fig. 8(f)). Thus, as r increased, the basal texture feature gradually changed to the off-basal texture feature, which greatly enhanced the basal slip activity and further improved the IE during the Erichsen cupping test [32–33]. Compared with the abovementioned features, GS and ΔS exhibited minimal influence on the SHAP value, which implies that both parameters are not the primary determinants of the stretch formability of Mg alloys. As reported by Nakata and Kamado [34], although the difference in GS was depicted differently in various Mg series alloys, evident evidence of grain refinement effect was not observed on the enhanced stretch formability. Based on the above critical values, we can adjust the microstructural features to guide the design of high-formable Mg alloys.

3.3.2. XGBoost feature importance assessment

Meanwhile, the XGBoost feature importance analysis was also performed. Fig. 9(a) shows the overall importance ranking characterized by a pie chart. The analysis results are consistent with those obtained via the SHAP method, with the top six screening factors (I_{max}, TYS, EL, r, ΔS, and GS). The next features were t, A, v, and μ. As a consequence of disparate measurement standards, the ranking of feature importance varied between the two analysis methods. The former is typically based on the evaluation of the overall model performance, and the latter relies on the evaluation of the local interpretability for each sample. Fig. 9(b)–(k) provides a detailed view of the relationships between individual features (I_{max}, TYS, EL, r, ΔS, GS, t, A, v, and μ) and IE, offering insights into the mechanism underlying the influence of each feature on the target variable. Evidently, with the gradual decrease in I_{max} and TYS and increase in EL, r, ΔS, and GS, the IE value showed an upward tendency. Compared with the top six screening factors, t, A, v, and μ showed a weak effect on the IE. Therefore, the integration of the SHAP method and XGBoost feature importance analysis confirmed the pivotal features and their quantitative influence on the stretch formability of AZ31 alloy sheets in this study.

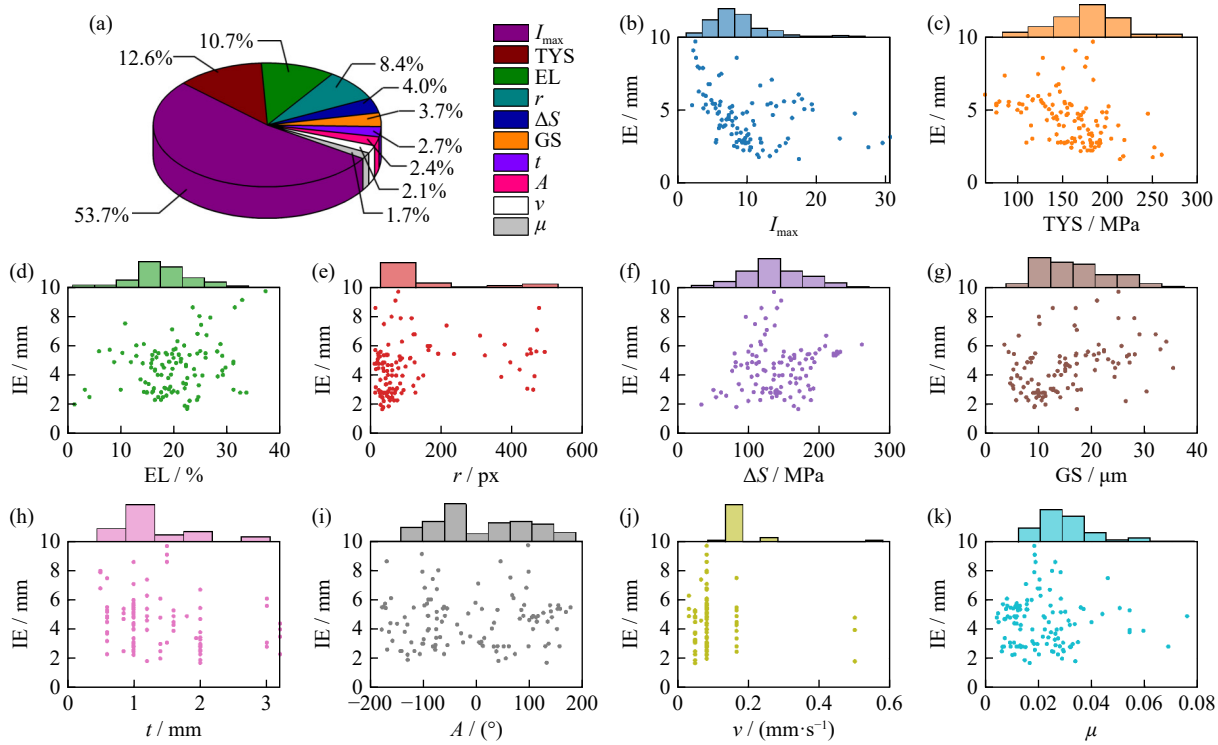

Fig. 9. (a) XGBoost importance proportion of each feature. Joint scatter plots revealing the relationship between the IE and different features: (b) I_{max}; (c) TYS; (d) EL (e) r; (f) ΔS; (g) GS; (h) t; (i) A; (j) v; (k) μ.

3.4. Verification via experiments

To validate the reliability and generalization performance of the SSA-XGBoost model, we prepared a new dataset comprising four samples (labeled by R0, R30, RA0, and RA30), and their corresponding microstructural features are shown in Fig. 10. All samples exhibited a relatively uniform grain structure. The R0 sample was a typical basal-oriented feature with the *c*-axis of the majority of grains exhibiting a slight inclination of approximately 7° from the ND to the RD in the (0001) pole figure (Fig. 10(a)), and its mean GS was approximately 22.1 μm (Fig. 10(e)). For the R30 sample, the *c*-axis of most grains located at around the 37° position away from the ND toward the RD in the (0001) pole figure (Fig. 10(b)). The mean GS showed no change (about 22.3 μm, Fig. 10(f)) compared with the R0 sample. No difference was observed in the texture type between the samples before and after annealing. However, the I_{max} was weakened from 14.1 (R0) and 11.5 (R30) to 12.0 (RA0) and 10.3 (RA30), as shown in Fig. 10(a)–(d). Meanwhile, the mean GS increased to 37.2 and 36.9 μm for the RA0 and RA30 samples displayed in Fig. 10(g) and (h), respectively. In addition to GS and I_{max}, other characteristics, e.g., μ, r, and A, for all samples are summarized in Table 1.

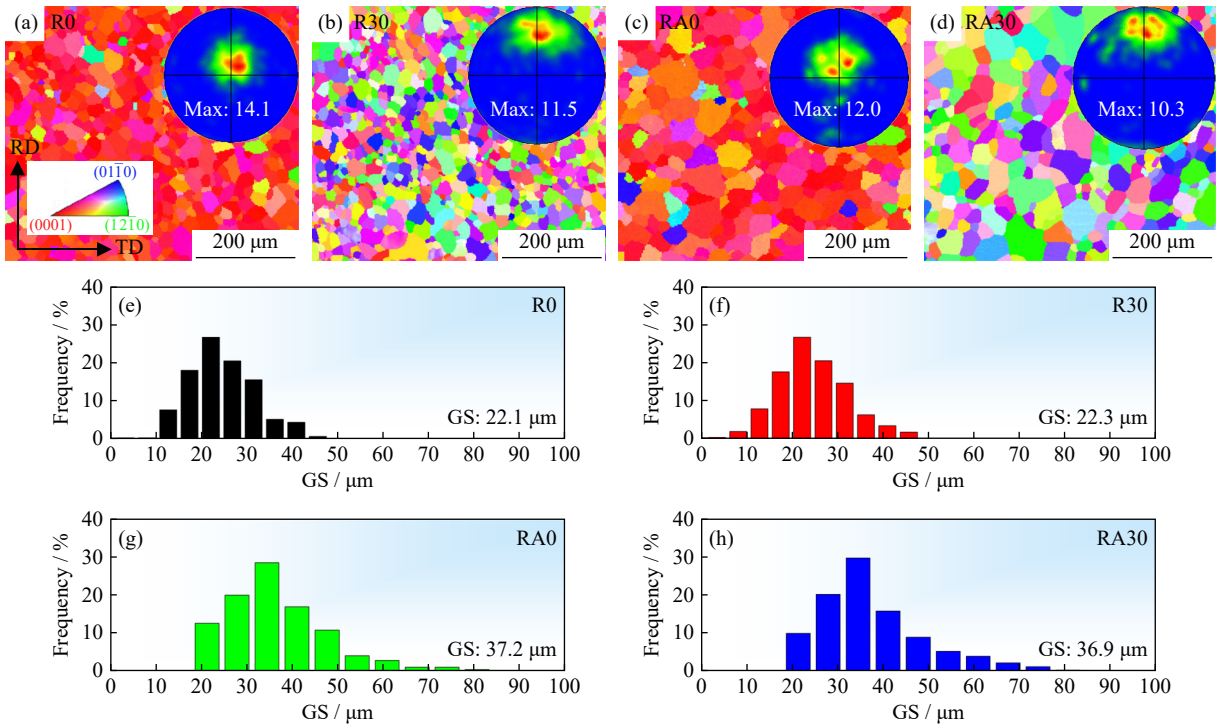

Fig. 10. (a–d) EBSD analysis (showing inverse pole figures and (0001) pole figures) and (e–h) GS distribution maps for R0, R30, RA0, and RA30 samples, respectively.

Table 1. Input and output parameters of validation samples

Sample	GS / μm	I_{max}	r / px	μ	A / (°)	TYS / MPa	EL / %	ΔS / MPa	t / mm	v / (mm·s^{-1})	IE (Experimental) / mm	IE (Prediction) / mm
R0	22.1	14.1	85.60	0.008	52.60	117.77	14.29	116.47	1	0.05	2.81	3.06
R30	22.3	11.5	302.29	0.011	85.46	69.39	23.48	151.07	1	0.05	6.54	6.32
RA0	37.2	12.0	112.80	0.009	60.95	107.63	14.73	121.23	1	0.05	3.36	3.32
RA30	36.9	10.3	300.43	0.010	86.95	61.62	25.34	152.13	1	0.05	6.92	6.73

Fig. 11(a)–(d) shows the engineering tensile stress–strain curves of each sample measured at 0°, 45°, and 90° away from the ND to the RD. Table 1 provides the corresponding average tensile properties. A strong basal texture resulted in the high TYS and low EL of the R0 sample (Fig. 11(a)). However, given the tensile "soft" orientations (especially for those at 0° and 45°), which are conducive to the activation of the basal slip system, the R30 sample showed a low TYS and a high EL (Fig. 11(b)). After annealing, further weakening of the basal texture contributed to a lower TYS and a higher EL of the RA0 and RA30 samples (Figs. 11(c) and (d)) compared with the R0 and R30 samples, which abided by Schmid's law very well [31,35–37]. In spite of the grain growth in the RA0 and RA30 samples, the positive effect of texture weakening on the enhanced EL value exceeded the negative influence of grain coarsening on them.

At given Erichsen cupping test conditions, e.g., t of 1 mm and v of 0.05 mm/s, the Erichsen results of the R0, R30, RA0, and RA30 samples were obtained (Fig. 11(e) and (f)). The corresponding IE acquired in the experiment and model prediction is labeled in Table 1. The RA30 sample exhibited the highest IE of 6.92 mm, followed by R30, RA0, and R0

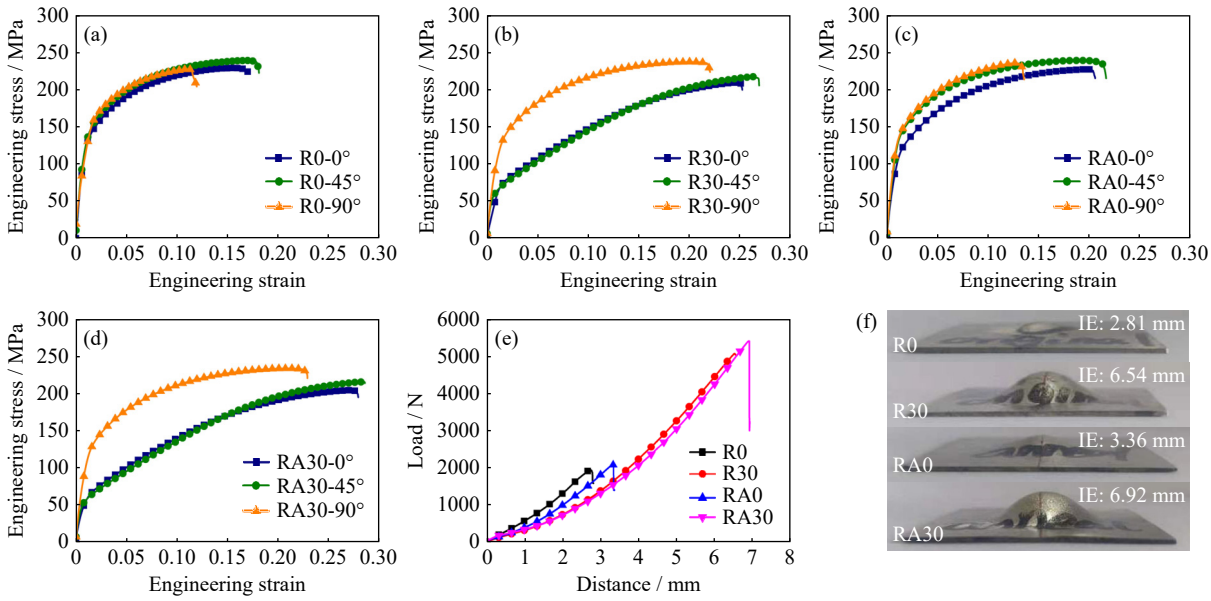

Fig. 11. Engineering tensile stress–strain curves of (a) R0, (b) R30, (c) RA0, and (d) RA30 samples; (e) Erichsen cupping test curves and (f) Erichsen cupping appearances of the samples.

samples, with values of 6.54, 3.36, and 2.81 mm, respectively. The discrepancy between the experimental and predicted IE was minimal, with a difference below 5%. This result indicates considerable potential for the quantitative prediction of the stretch formability of AZ31 alloy sheets via the newly developed SSA-XGBoost model. Combining the microstructural features and mechanical properties, we observed that with the decrease in I_{max} and average TYS, the IE showed a rising tendency, but it decreased with the decrease in the average EL. Thus, the I_{max}, TYS, and EL are the three key factors in this dataset that influenced the stretch formability of AZ31 alloy sheets, consistent with results of the SHAP method and XGBoost feature importance analysis (Figs. 8 and 9).

In addition, other features, such as r and GS, contributed to the overall effect. As the r increased, more $\{10\bar{1}2\}$ extension twins were activated, as revealed by the "S"-shaped stress–strain curves of the R30 and RA30 samples tensioned along the angles of 0° and 45° (Fig. 11(b) and (d)), providing better coordination for the thickness-direction strains. However, given the formation of off-basal texture, an evident tensile planar anisotropy, which is harmful to the enhancement of IE, was observed [38]. If we consider the effect of individual GS on stretch formability, twins can be easily activated in large grains to compensate for extra strains and increase the IE [9–10], which is also confirmed in the R0 and RA0 samples (Fig. 11(a) and (c)). Once other factors, except for GS, appear, such a proportional relationship may be invalid [39–41]. As shown in Fig. 10(a) and (b), despite a comparable average GS between the R0 and R30 samples, a notable discrepancy in the IE value was evident due to variation in the r value.

The developed SSA-XGBoost algorithm exhibited considerable potential in forecasting the stretch formability of AZ31 alloy sheets and quantitatively analyzing the key features of the IE value. This work offers insights into the development of high-formable Mg alloys.

4. Conclusions

This work involved the development of an interpretable prediction framework that comprehensively considers microstructures, mechanical properties, and testing conditions for the accurate prediction of the stretch formability of AZ31 Mg alloys. In addition, the relationship between some key variables and the IE was quantitatively analyzed. The findings are expected to provide guidance on the design of Mg alloys with high formability via this model. The main conclusions are as follows:

(1) The inputs for the model included 11 features, which were divided into three categories: (a) microstructures, e.g., GS, I_{max}, μ, r, and A; (b) mechanical properties, e.g., TYS, UTS, EL, and ΔS; (c) test conditions, e.g., t and v. Through the PCC and ES methods, ten key features (excluding UTS), as the final inputs, were determined to improve the prediction accuracy of the model.

(2) Compared with the conventional XGBoost, ANN, LSTM, SVM, RF, and RT algorithms, the newly developed SSA-XGBoost model exhibited a higher prediction accuracy with an R^2 value of 0.91 while ensuring the model robustness.

(3) As revealed by the SHAP method and XGBoost feature importance analysis, the I_{max}, TYS, EL, r, GS, and ΔS significantly influenced the stretch formability of input features. When $I_{max} < 6.1$, TYS < 150 MPa, EL > 22.6%, and r > 127 px, the IE displayed an upward tendency. Compared with I_{max}, TYS, EL, and r, GS and ΔS exhibited a relatively weak effect on the IE.

(4) The SSA-XGBoost model was further validated under actual experimental conditions, with the error of IE value remaining within 5%. The predicted results demonstrated good agreement with the experimental data, which confirms the effectiveness and potential application of the SSA-XGBoost

model in the prediction of the stretch formability of AZ31 Mg alloys.

Acknowledgements

This research was funded by the National Natural Science Foundation of China (No. 52204407), the Natural Science Foundation of Jiangsu Province, China (No. BK20220595), the China Postdoctoral Science Foundation (No. 2022M 723689), and the Postgraduate Research & Practice Innovation Program of Jiangsu Province, China (No. SJCX23_ 1913).

Conflict of Interest

Bin Jiang is an editorial board member for this journal and was not involved in the editorial review or the decision to publish this article. All authors certify that they have no affiliations with or involvement in any organization or entity with any financial interest or non-financial interest in the subject matter or materials discussed in this manuscript.

Supplementary Information

The online version contains supplementary material available at https://doi.org/10.1007/s12613-024-3002-9.

References

[1] J.Y. Zhang, J.S. Miao, N. Balasubramani, *et al*., Magnesium research and applications: Past, present and future, *J. Magnesium Alloys*, 11(2023), No. 11, p. 3867.

[2] Q.H. Wang, B. Jiang, D.L. Chen, *et al*., Strategies for enhancing the room-temperature stretch formability of magnesium alloy sheets: A review, *J. Mater. Sci.*, 56(2021), No. 23, p. 12965.

[3] J.R. Dong, D.F. Zhang, J. Sun, Q.W. Dai, and F.S. Pan, Effects of different stretching routes on microstructure and mechanical properties of AZ31B magnesium alloy sheets, *J. Mater. Sci. Technol.*, 31(2015), No. 9, p. 935.

[4] T.T. Trang, J.H. Zhang, J.H. Kim, *et al*., Designing a magnesium alloy with high strength and high formability, *Nat. Commun.*, 9(2018), No. 1, art. No. 2522.

[5] A. Dutta, I. Charit, L.B. Johannes, and R.S. Mishra, Deep cup forming by superplastic punch stretching of friction stir processed 7075 Al alloy, *Mater. Sci. Eng. A*, 395(2005), No. 1-2, p. 173.

[6] Y.J. Wang, Y. Zhang, and H.T. Jiang, Tension: Compression asymmetry and corresponding deformation mechanism in ZA21 magnesium bars with bimodal structure, *Int. J. Miner. Metall. Mater.*, 30(2023), No. 1, p. 92.

[7] X.S. Huang, K. Suzuki, and Y. Chino, Influences of initial texture on microstructure and stretch formability of Mg–3Al–1Zn alloy sheet obtained by a combination of high temperature and subsequent warm rolling, *Scripta Mater.*, 63(2010), No. 4, p. 395.

[8] Q.S. Yang, B. Jiang, B. Song, *et al*., The effects of orientation control *via* tension-compression on microstructural evolution and mechanical behavior of AZ31 Mg alloy sheet, *J. Magnesium Alloys*, 10(2022), No. 2, p. 411.

[9] D.H. Kang, D.W. Kim, S. Kim, G.T. Bae, K.H. Kim, and N.J. Kim, Relationship between stretch formability and work-hardening capacity of twin-roll cast Mg alloys at room temperature, *Scripta Mater.*, 61(2009), No. 7, p. 768.

[10] J.W. Park and K.S. Shin, Improved stretch formability of AZ31 sheet via grain size control, *Mater. Sci. Eng. A*, 688(2017), p. 56.

[11] K. Wei, R. Hu, D.D. Yin, *et al*., Grain size effect on tensile properties and slip systems of pure magnesium, *Acta Mater.*, 206(2021), art. No. 116604.

[12] H.B. Hou, J.F. Wang, L. Ye, S.J. Zhu, L.G. Wang, and S.K. Guan, Prediction of mechanical properties of biomedical magnesium alloys based on ensemble machine learning, *Mater. Lett.*, 348(2023), art. No. 134605.

[13] S.J. Huang, M.P. Mose, and S. Kannaiyan, A study of the mechanical properties of AZ61 magnesium composite after equal channel angular processing in conjunction with machine learning, *Mater. Today Commun.*, 33(2022), art. No. 104707.

[14] X.N. Xu, L.Y. Wang, G.M. Zhu, and X.Q. Zeng, Predicting tensile properties of AZ31 magnesium alloys by machine learning, *JOM*, 72(2020), No. 11, p. 3935.

[15] Y.B. Zhang, S.W. Bai, B. Jiang, K. Li, Z.H. Dong, and F.S. Pan, Modeling the correlation between texture characteristics and tensile properties of AZ31 magnesium alloy based on the artificial neural networks, *J. Mater. Res. Technol.*, 24(2023), p. 5286.

[16] E.J. Schiessler, T. Würger, S.V. Lamaka, *et al*., Predicting the inhibition efficiencies of magnesium dissolution modulators using sparse machine learning models, *npj Comput. Mater.*, 7(2021), art. No. 193.

[17] Y.W. Wang, T. Xie, Q.L. Tang, *et al*., High-throughput calculations combining machine learning to investigate the corrosion properties of binary Mg alloys, *J. Magnesium Alloys*, 12(2024), No. 4, p. 1406.

[18] Z.X. Lu, S.J. Si, K.Y. He, *et al*., Prediction of Mg alloy corrosion based on machine learning models, *Adv. Mater. Sci. Eng.*, 2022(2022), art. No. 9597155.

[19] T.Z. Xin, S. Tang, F. Ji, *et al*., Phase transformations in an ultralight BCC Mg alloy during anisothermal ageing, *Acta Mater.*, 239(2022), art. No. 118248.

[20] J. Suh, J. Victoria-Hernández, D. Letzig, R. Golle, and W. Volk, Effect of processing route on texture and cold formability of AZ31 Mg alloy sheets processed by ECAP, *Mater. Sci. Eng. A*, 669(2016), p. 159.

[21] D. Ren, C.C. Wang, X.L. Wei, Q.Q. Lai, and W. Xu, Building a quantitative composition-microstructure-property relationship of dual-phase steels via multimodal data mining, *Acta Mater.*, 252(2023), art. No. 118954.

[22] R.H. Yuan, Z. Liu, P.V. Balachandran, *et al*., Accelerated discovery of large electrostrains in $BaTiO_3$-based piezoelectrics using active learning, *Adv. Mater.*, 30(2018), No. 7, art. No. 1702884.

[23] J. Su, Y.Z. Wang, X.K. Niu, S. Sha, and J.Y. Yu, Prediction of ground surface settlement by shield tunneling using XGBoost and Bayesian Optimization, *Eng. Appl. Artif. Intell.*, 114(2022), art. No. 105020.

[24] L.X. Liu, X. Wang, X. Yang, H.J. Liu, J.P. Li, and P.F. Wang, Path planning techniques for mobile robots: Review and prospect, *Expert Syst. Appl.*, 227(2023), art. No. 120254.

[25] M.Z. Sun, J.M. Yang, C.Y. Yang, W.P. Wang, X.B. Wang, and H.F. Li, Research on prediction of PPV in open-pit mine used RUN-XGBoost model, *Heliyon*, 10(2024), No. 7, art. No. e28246.

[26] L.F. Zhu, Q. Luo, Q.C. Chen, *et al*., Prediction of ultimate tensile strength of Al–Si alloys based on multimodal fusion learning, *Mater. Genome Eng. Adv.*, 2(2024), No. 1, art. No. e26.

[27] H.T. Zhang, H.D. Fu, S.C. Zhu, W. Yong, and J.X. Xie, Machine learning assisted composition effective design for precipitation strengthened copper alloys, *Acta Mater.*, 215(2021), art.

No. 117118.
[28] H.M. Zhou, L.S. Ma, X.L. Niu, *et al*., A novel hybrid model combined with ensemble embedded feature selection method for estimating reference evapotranspiration in the North China Plain, *Agric. Water Manage.*, 296(2024), art. No. 108807.
[29] B. Nenchev, Q. Tao, Z.H. Dong, *et al*., Evaluating data-driven algorithms for predicting mechanical properties with small datasets: A case study on gear steel hardenability, *Int. J. Miner. Metall. Mater.*, 29(2022), No. 4, p. 836.
[30] Y. Chino, K. Kimura, and M. Mabuchi, Deformation characteristics at room temperature under biaxial tensile stress in textured AZ31 Mg alloy sheets, *Acta Mater.*, 57(2009), No. 5, p. 1476.
[31] Q.H. Wang, B. Jiang, A.T. Tang, *et al*., Formation of the elliptical texture and its effect on the mechanical properties and stretch formability of dilute Mg–Sn–Y sheet by Zn addition, *Mater. Sci. Eng. A*, 746(2019), p. 259.
[32] C. He, H.R. Zhu, M. Yuan, *et al*., Comparison of room-temperature stretch formability of the as extruded Mg–Gd alloys with different double-peak pole spacing, *J. Mater. Res. Technol.*, 15(2021), p. 4838.
[33] M. Panchal, L. Kaushik, M.S. Kim, R.K. Renganayagalu, S.H. Choi, and J. Singh, Effect of pre-twinning and heat treatment on formability of AZX311 Mg alloy, *J. Magnesium Alloys*, 12(2024), No. 3, p. 1154.
[34] T. Nakata and S. Kamado, Towards tailoring basal texture of rolled Mg alloy sheet by recrystallization for high room-temperature formability: A review, *J. Magnesium Alloys*, 11(2023), No. 11, p. 3992.
[35] J. Suh, J. Victoria-Hernandez, D. Letzig, *et al*., Improvement in cold formability of AZ31 magnesium alloy sheets processed by equal channel angular pressing, *J. Mater. Process. Technol.*, 217(2015), p. 286.
[36] J. Tu, T. Zhou, L. Liu, *et al*., Effect of rolling speeds on texture modification and mechanical properties of the AZ31 sheet by a combination of equal channel angular rolling and continuous bending at high temperature, *J. Alloy. Compd.*, 768(2018), p. 598.
[37] J. Xu, J. Zhao, B. Jiang, *et al*., Effect of transverse gradient extrusion process on texture and mechanical properties of Mg–3Al–1Zn alloy sheets, *J. Mater. Res. Technol.*, 27(2023), p. 6171.
[38] M.M. Hoseini-Athar, R. Mahmudi, R.P. Babu, and P. Hedström, Tailoring the texture of an extruded Mg sheet through constrained groove pressing for achieving low mechanical anisotropy and high yield strength, *Scripta Mater.*, 186(2020), p. 253.
[39] Q.H. Wang, J.F. Song, B. Jiang, *et al*., An investigation on microstructure, texture and formability of AZ31 sheet processed by asymmetric porthole die extrusion, *Mater. Sci. Eng. A*, 720(2018), p. 85.
[40] Z.R. Zeng, J.F. Nie, S.W. Xu, C.H.J. Davies, and N. Birbilis, Super-formable pure magnesium at room temperature, *Nat. Commun.*, 8(2017), No. 1, art. No. 972.
[41] H. Somekawa, A. Kinoshita, and A. Kato, Great room temperature stretch formability of fine-grained Mg–Mn alloy, *Mater. Sci. Eng. A*, 697(2017), p. 217.